Elementary Clothoid-based 3D curve for Unmanned Aerial Vehicles

Leopoldo Armesto* and Gloria Vanegas†
Polytechnic University of Valencia (Universitat Politècnica de València), València, 46022, Spain

Vicent Girbés-Juan‡
University of Valencia (Universitat de València), Burjassot, 46100, Spain

I. Introduction

UNMANNED Aerial Vehicles (UAVs), either multi-rotor or fixed-wing UAVs, can be used in many fields to solve complex problems in safety [1], communications [2, 3], military applications [4, 5], civilian applications [6, 7], protection of nuclear plants [8], energy efficiency [9], nonlinear control [10, 11] and path planning [12], among others. Vertical Take Off and Landing (VTOL) is by far the most used UAV's configuration [13]. Probably the main reason is that, nowadays, there are lots of low cost multi-rotor models. VTOL strategies can be applied to fixed-wing airplanes [14], however in normal operation they usually fly horizontally to keep a constant altitude [15, 16], but they need to perform changes in their heading and altitude very often, specially in cluttered environments [17].

One approach to deal with navigation problems of UAVs is from the point of view of optimization and control theory. In [18], a model predictive convex programming (MPCP) for constrained vehicle guidance was developed. Compared to model predictive static programming methods, it offers the advantage of considering state and input constraints as well as choosing the cost function. The same authors have recently used trigonometric series for UAV path planning [19]. In this work a computationally efficient trajectory is generated for smooth aircraft flight level changes. It uses convex-optimization based on linearizations of the dynamics.

A second approach to solve navigation applications is from the trajectory planning point of view. In [20], the authors proposed a curvature continuous and bounded path planning method for UAVs considering kinematic and dynamic constraints such as maximum velocity and curvature. Indeed, they proposed the use of Bézier curves as transition curves, but this type of spatial curve has no physical meaning and it is hard to get the relationship between its parameters and vehicle's physics (kinematics and dynamics). Pythagorean Hodographs are also well extended for UAV planning, but they require to solve an optimization problem in order to take constraints into account [21, 22]. Among other spatial curves, clothoids (also known as Euler or Cornu Spirals) play an important role, because of their "nice" geometric properties, including a close relation between physical phenomena (normal acceleration and jerks) with the clothoid scaling parameter. Therefore, borrowing the idea from the planar movement, spatial clothoids could be used in Path

---

*Lecturer, Control Systems and Engineering Department, larmesto@idf.upv.es.
†PhD. student, Control Systems and Engineering Department, glovaza@doctor.upv.es.
‡Assistant Professor, Electronics Engineering Department, vicent.girbes@uv.es.

Planning [23, 24].

Clothoids have been studied deeply in ground mobile robotics [24–29]. For instance, in [30–32] the authors showed that the use of clothoids as transition curves not only guaranteed continuous curvature (G^2 continuity) but also a bound on its derivative, the sharpness. So, when the tracking speed is constant, the normal acceleration is bounded if the maximum curvature and its derivative are bounded. In order to increase driving safety and comfort in road design, many studies have been done to determine appropriate values for clothoid sharpness in transition curves [33, 34]. Indeed, clothoids are usually used in highway, railway and roller coasters design [35], among other applications. Recent works proved that including comfort and safety requirements in the path planning process can avoid tip-overs in forklifts carrying heavy loads at high speeds [27, 28].

Even though the benefits of planar clothoids have been proven, researchers have paid little attention to the use of such curves in the 3D space [36]. A few works proposed the use of clothoids in path planning for UAVs [37]. Others instead, approached a similar problem from the field of computer graphics [23]. Nevertheless, only one seems to match with the exact definition of a 3D clothoid [38]. But, the problem is that this approach is based on a Frenet-Serret frame and requires a numeric integration to be computed. Moreover, since they are generated from the linear equations of curvature and torsion, it is not possible to know *a priori* the increment in position and orientation with respect to the origin of the curve.

A new spatial clothoid-based 3D curve is proposed in this Note. The new curve is built with two clothoid-based three-dimensional curves (Cb3D) [24] and inherits many of their interesting properties, such as smoothness, scaling and symmetry, for path planning methods. The main contribution with respect to our previous work is the fact that, with the new curve definition, we can join line segments pointing towards arbitrary target directions. Thus, it can be used as a transition curve for many path planning methods for UAVs [39]. In addition to this, we show how to compute the parameters of the new curve, as well as analyze the conditions in which the monotonicity property holds. It's important to remark that constraints on the maximum sharpness of curvature and torsion are considered in this approach. In summary, Cb3D curves represent the tool on which our new proposal is based on, while this Note proposes the proper combination of two of them to actually build a transition curve with application to UAVs, resembling a 3D extension to Elementary paths [40] used in car-like vehicles.

The Note is organized as follows. Section II provides some preliminaries as well as states the problem to be solved. In Section III the proposed curve is defined, and it shows curve properties such as smoothness, scalability, and symmetry, among others. Section IV conducts an analysis of the target angles region where the curve increases monotonically in position and orientation. Section V describes the proposed design methodology to obtain the shortest possible curve satisfying parameter constraints and shows a case study, a comparison with 3D pure clothoids and its application to fixed-wing UAVs in orientation heading and altitude change problem. At the end of the Note, we discuss the application and advantages of the proposed method in Section VI and draw some conclusions in Section VII.

II. Preliminaries

A. Clothoid-Based Three-Dimensional Curve (Cb3D)

In [24] a new clothoid-based three-dimensional curve (Cb3D) is defined as a composition of two planar clothoids. The authors proposed that each clothoid is contained in a plane orthogonal to each other (clothoids are defined in planes XY and XZ). The clothoid contained in plane XY is indeed a clothoid whose length depends on the clothoid on plane XZ. In [24], this curve is used as a reference trajectory to control a fixed-wing UAV.

Let $\mathbf{C}_1(q, \mu) := [C(q, \mu) \; \mathcal{S}(q, \mu)]^T \in \mathbb{R}^2$ be a planar clothoid contained in plane XY with arc-length q, being μ the clothoid's curvature sharpness; and $\mathbf{C}_2(w, \rho) := [C(w, \rho) \; \mathcal{S}(w, \rho)]^T \in \mathbb{R}^2$ another planar clothoid contained in plane XZ with arc-length w and torsion sharpness ρ, both defined by Fresnel integrals $C(s, \sigma) = \int_0^s \cos(\frac{\sigma}{2}\xi^2)\, d\xi$ and $\mathcal{S}(s, \sigma) = \int_0^s \sin(\frac{\sigma}{2}\xi^2)\, d\xi$.

A Cb3D curve can be generated as a composition of both planar clothoids [24] as follows:

$$\mathbf{C}(s, \mu, \rho) := \left[C(C(s, \rho), \mu) \quad \mathcal{S}(C(s, \rho), \mu) \quad -\mathcal{S}(s, \rho) \right]^T, \tag{1}$$

while its pitch $\theta(s, \rho)$ and yaw $\Psi(s, \mu, \rho)$ angles can be computed as

$$\theta(s, \rho) = \frac{\rho}{2}s^2, \quad \Psi(s, \mu, \rho) = \frac{\mu}{2}C^2(s, \rho), \tag{2}$$

and its tangent vector is

$$\mathbf{T}(s, \mu, \rho) := \left[\cos(\Psi(s, \mu, \rho))\cos(\theta(s, \rho)) \quad \sin(\Psi(s, \mu, \rho))\cos(\theta(s, \rho)) \quad -\sin(\theta(s, \rho)) \right]^T. \tag{3}$$

Thus, given an arbitrary target tangent vector $\mathbf{T}^*$, defined by final angles $\theta^* \in [-\pi/2, \pi/2]$ rad and $\Psi^* \in [-\pi, \pi]$ rad, and arc-length $s > 0$, there is only one pair of parameters μ^* and ρ^* that synthesize a Cb3D curve [24]:

$$\rho^* = \frac{2\theta^*}{s^2} \tag{4}$$

$$\mu^* = \frac{2\Psi^*}{C^2(s, \rho^*)} \tag{5}$$

B. Problem Statement

The aim is to generate a path $\mathbf{E}(s, \mathbf{p})$, where $\mathbf{p} = \{\mu, \; \rho\}$ are curve specific parameters (curvature and torsion sharpness) and $s \in [0, S]$ is the curve length. Parameters $\mathbf{p}$ are assumed to be constrained, i.e.: $\mu \in [-\mu_{max}, \mu_{max}]$ and $\rho \in [-\rho_{max}, \rho_{max}]$. For a given initial configuration with null curvature and torsion, the path must point towards a given relative direction $\mathbf{T}^*$, that is, $\mathbf{T}^* = \frac{\mathbf{E}'(S, \mathbf{p})}{\|\mathbf{E}(S, \mathbf{p})\|}$. Without loss of generality, it can be assumed that the UAV is centered

at the origin and its initial orientation is also zero (local and global coordinate frames are coincident), otherwise we can always apply a transformation to obtain a local target direction. We also assume that a low-level controller ensures that the UAV follows that path and thus, the design of such low-level controller is out of the scope of this Note.

III. Elementary Clothoid-based 3D curve: Definition and Properties

In the planar case, the concept of *Elementary Path* was introduced by Fraichard and Scheuer [40], as a combination of two symmetrical 2D clothoids with the same sharpness and length. In this sense, the work presented in this Note extends this idea to 3D space, combining two Cb3D curves. An Elementary Clothoid-based 3D curve (ECb3D or Elementary for short) can be defined, for $s \in [-S, S]$ and $\tilde{s} > 0$ as:

$$\mathbf{E}(s, \tilde{s}, \mathbf{p}) := \begin{cases} \mathbf{C}(s, \mathbf{p}) & if \ |s| \le \tilde{s} \\ \tilde{\mathbf{C}}(s, \tilde{s}, \mathbf{p}) & \text{otherwise} \end{cases} \qquad (6)$$

with $\tilde{s}$ the length of each Cb3D curve (referred here as *primary* and *secondary* curves), S is the overall Elementary length and thus, by definition, $S := 2\tilde{s}$, and Cb3D sharpness parameters are $\mathbf{p} = \{\mu, \rho\}$. The *secondary* Cb3D is indeed a rotated and translated Cb3D curve as follows:

$$\tilde{\mathbf{C}}(s, \tilde{s}, \mathbf{p}) = \mathbf{R}_{\mathbf{T}(\tilde{s}, \mathbf{p})}(\pi) \left(\mathbf{C}(s - \text{sign}(s)2\tilde{s}, \mathbf{p}) + \text{sign}(s)\mathbf{C}(\tilde{s}, \mathbf{p}) \right) + \text{sign}(s)\mathbf{C}(\tilde{s}, \mathbf{p}), \qquad (7)$$

being $\mathbf{R}_{\mathbf{T}(\tilde{s}, \mathbf{p})}(\pi)$ a rotation of π around vector $\mathbf{T}(\tilde{s}, \mathbf{p})$, that is, based on Rodrigues formula [41] we have:

$$\mathbf{R}_{\mathbf{T}(\tilde{s}, \mathbf{p})}(\pi) = \cos \pi \mathbf{I}_{3\times3} + (1 - \cos \pi)\mathbf{T}(\tilde{s}, \mathbf{p})\mathbf{T}^T(\tilde{s}, \mathbf{p}) + \sin(\pi)\left[\mathbf{T}(\tilde{s}, \mathbf{p})_\times \right] = 2\mathbf{T}(\tilde{s}, \mathbf{p})\mathbf{T}^T(\tilde{s}, \mathbf{p}) - \mathbf{I}_{3\times3}, \qquad (8)$$

being $\left[\mathbf{T}(\tilde{s}, \mathbf{p})_\times \right]$ a skew-symmetric matrix.

Figure 1 shows a representative ECb3D curve with its 4 possible cases, i.e., combinations of positive and negative values of the clothoid parameters. The *primary clothoid* $\mathbf{C}(s, \mathbf{p})$, painted in solid line, is a Cb3D curve evaluated for $|s| \le \tilde{s}$ and it can be computed for positive or negative s, while $\tilde{s}$ is the length of such primary clothoid. On the other hand, the *secondary clothoid*, $\tilde{\mathbf{C}}(s, \tilde{s}, \mathbf{p})$, painted in a dashed line, is another Cb3D curve properly rotated and translated to ensure position continuity as well as coincident tangent vectors for $s = \tilde{s}$, i.e. the curve has G^1 continuity by definition. Note that in Fig. 1 the colored frame axis at the origin have been depicted too for reference. By convenience, and abusing of notation, we will drop the last arguments of expressions if it is clear from the context, i.e.: $\mathbf{E}(s, \tilde{s}, \mathbf{p})$ might be expressed as $\mathbf{E}(s, \tilde{s})$ or even $\mathbf{E}(S)$ for the particular case when $s = S = 2\tilde{s}$. Similarly, $\mathbf{C}(s, \mathbf{p})$ can be expressed as $\mathbf{C}(s)$.

Lemma III.1 (Smoothness) *An Elementary clothoid-based 3D curve is C^∞ smooth with $\mu \neq 0$ or $\rho \neq 0$ for*
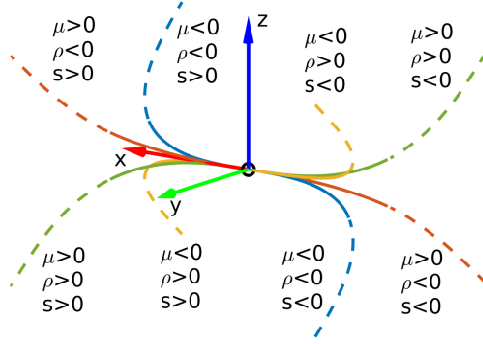
4

Fig. 1 **Elementary Clothoid-based 3D curves, all 4 possible cases based on clothoid parameters, with *Primary clothoids* in solid lines and *secondary clothoids* in dashed lines.**

$s \in [-2\tilde{s}, 2\tilde{s}]$ *and* $\tilde{s} > 0$*. Indeed, the n-th derivative can be computed as a piece-wise function as follows:*

$$\mathbf{E}^{(n)}(s, \tilde{s}, \mathbf{p}) := \begin{cases} \mathbf{C}^{(n)}(s, \mathbf{p}) & if \ |s| \leq \tilde{s} \\ \\ \mathbf{R}_{\mathbf{T}(\tilde{s}, \mathbf{p})}(\pi)\mathbf{C}^{(n)}(s - 2\tilde{s}, \mathbf{p}) & otherwise \end{cases}, \tag{9}$$

where $\mathbf{C}^{(n)}(s, \mathbf{p})$ *is a vector with trigonometric expressions:*

$$\mathbf{C}^{(n)}(s, \mathbf{p}) = \begin{bmatrix} \tilde{d}_{1,n} \cos \Psi(s) \cos \theta(s) + \tilde{d}_{2,n} \sin \Psi(s) \cos \theta(s) + \tilde{d}_{3,n} \cos \Psi(s) \sin \theta(s) + \tilde{d}_{4,n} \sin \Psi(s) \sin \theta(s) \\ \bar{d}_{1,n} \cos \Psi(s) \cos \theta(s) + \bar{d}_{2,n} \sin \Psi(s) \cos \theta(s) + \bar{d}_{3,n} \cos \Psi(s) \sin \theta(s) + \bar{d}_{4,n} \sin \Psi(s) \sin \theta(s) \\ \hat{d}_{1,n} \sin \theta(s) + \hat{d}_{2,n} \cos \theta(s) \end{bmatrix}, \tag{10}$$

for some polynomials $\tilde{d}_{1,n}$, $\tilde{d}_{2,n}$, $\tilde{d}_{3,n}$, $\tilde{d}_{4,n}$, $\bar{d}_{1,n}$, $\bar{d}_{2,n}$, $\bar{d}_{3,n}$, $\bar{d}_{4,n}$, $\hat{d}_{1,n}$ *and* $\hat{d}_{2,n}$*; and pitch and yaw angles are given by Eq.* (2) *, where parameters* μ *and* ρ *are omitted to simplify notation.*

Proof The proof is made for $s > 0$, but equivalent proof can be made for $s < 0$. A C^∞ function is differentiable for all degrees of differentiation; that is, its position vector can be derived ∞ times. Since an Elementary curve is a piece-wise function, its derivatives can be computed for $s < \tilde{s}$ and $s > \tilde{s}$ and recalling the smoothness property of a Cb3D curve in [24], we can clearly see that $\mathbf{E}^{(n)}(s, \tilde{s}) = \mathbf{C}^{(n)}(s)$ is C^∞ for $s < \tilde{s}$ and also is C^∞ for $s > \tilde{s}$ due to $\mathbf{E}^{(n)}(s, \tilde{s}) = \tilde{\mathbf{C}}^{(n)}(s, \tilde{s})$, where $\tilde{\mathbf{C}}^{(n)}(s, \tilde{s}) = \mathbf{R}_{\mathbf{T}(\tilde{s})}(\pi)\mathbf{C}^{(n)}(s - 2\tilde{s})$ is a transformed Cb3D curve and thus the same property holds.

So, to complete the proof we need to check that the following limits exist:

$$\lim_{s \to \tilde{s}^-} \mathbf{E}^{(n)}(s, \tilde{s}) = \lim_{s \to \tilde{s}^+} \mathbf{E}^{(n)}(s, \tilde{s}). \tag{11}$$

In this sense, we can see that $\lim_{s \to \tilde{s}^-} \mathbf{E}^{(n)}(s, \tilde{s}) = \mathbf{C}^{(n)}(\tilde{s}, \tilde{s})$ and on the other hand:

$$\lim_{s \to \tilde{s}^+} \mathbf{E}^{(n)}(s, \tilde{s}) = \lim_{s \to \tilde{s}^+} \frac{\tilde{\mathbf{C}}^{(n-1)}(s, \tilde{s}) - \tilde{\mathbf{C}}^{(n-1)}(\tilde{s}, \tilde{s})}{s} = \mathbf{C}^{(n)}(\tilde{s}), \tag{12}$$

because $\lim_{s \to \tilde{s}^+} \frac{\tilde{\mathbf{C}}^{(n-1)}(s, \tilde{s}) - \tilde{\mathbf{C}}^{(n-1)}(\tilde{s}, \tilde{s})}{s} = \mathbf{R_T} \lim_{s \to \tilde{s}^+} \frac{\mathbf{C}^{(n-1)}(s - 2\tilde{s}) - \mathbf{C}^{(n-1)}(\tilde{s} - 2\tilde{s})}{s} = \mathbf{R_T} \mathbf{C}^{(n)}(-\tilde{s})$. Noting that $\theta(-\tilde{s}) = \theta(\tilde{s})$, $\Psi(-\tilde{s}) = \Psi(\tilde{s})$ and $\theta^{(n)}(-\tilde{s}) = -\theta^{(n)}(\tilde{s})$, $\Psi^{(n)}(-\tilde{s}) = -\Psi^{(n)}(\tilde{s})$ for $n = 1, 3, \ldots$, while $\theta^{(n)}(-\tilde{s}) = \theta^{(n)}(\tilde{s})$, $\Psi^{(n)}(-\tilde{s}) = \Psi^{(n)}(\tilde{s})$ for $n = 2, 4, \ldots$; and the fact that coefficients in Eq. (10) depend on polynomials of such derivatives of order $n - 1$ that are affected in such a way that also $\tilde{d}_{1,n}(-\tilde{s}) = -\tilde{d}_{1,n}(\tilde{s})$, $\tilde{d}_{2,n}(-\tilde{s}) = -\tilde{d}_{2,n}(\tilde{s})$, etc... for $n = 1, 3, \ldots$ and $\tilde{d}_{1,n}(-\tilde{s}) = \tilde{d}_{1,n}(\tilde{s})$, $\tilde{d}_{2,n}(-\tilde{s}) = \tilde{d}_{2,n}(\tilde{s})$, etc... for $n = 2, 4, \ldots$. As a consequence, we can express $\mathbf{C}^{(n)}(-\tilde{s}) = (-1)^{n-1} \mathbf{C}^{(n)}(\tilde{s})$ and therefore, $\mathbf{R_T} \mathbf{C}^{(n)}(-\tilde{s}) = (-1)^{n-1} \mathbf{R_T} \mathbf{C}^{(n)}(\tilde{s}) = \mathbf{C}^{(n)}(\tilde{s})$, because $\mathbf{C}^{(n)}(\tilde{s}) \parallel \mathbf{T}(\tilde{s})$ for $n = 1, 3, \ldots$ and $\mathbf{C}^{(n)}(\tilde{s}) \perp \mathbf{T}(\tilde{s})$ for $n = 2, 4, \ldots$ and thus $\mathbf{R_T}$ does not affect to cases $n = 1, 3, \ldots$ and changes the sign of $\mathbf{C}^{(n)}(\tilde{s})$ for $n = 2, 4, \ldots$, additional details have been omitted for brevity. ∎

Thus, Lemma III.1 states that the proposed curve is smooth, that is, their derivatives are differentiable. This is a desirable property in many path planning methods to ensure that control actions are also smooth [20]. In [24], the authors show that some kinematic-based and dynamic-based metrics such as linear and angular velocities, linear and angular accelerations, jerks, etc. are improved using this type of curves.

Lemma III.2 (Symmetry and Scalability) *An Elementary clothoid-based 3D curve is a symmetric and a scalable curve with scaling factor $\lambda > 0$ as follows:*

$$\mathbf{E}(s, \tilde{s}, \mathbf{p}) = -\mathbf{E}(-s, \tilde{s}, \mathbf{p}) \tag{13}$$

$$\lambda \mathbf{E}(s, \tilde{s}, \mathbf{p}) = \mathbf{E}(\lambda s, \lambda \tilde{s}, \lambda^{-2} \mathbf{p}). \tag{14}$$

Proof Let's recall the symmetry property of a Cb3D curve [24], that is $\mathbf{C}(s, \mathbf{p}) = -\mathbf{C}(-s, \mathbf{p})$, we have:

$$- \mathbf{E}(-s, \tilde{s}, \mathbf{p}) = \begin{cases} -\mathbf{C}(-s, \mathbf{p}) & if \ |s| \leq \tilde{s} \\ -\tilde{\mathbf{C}}(-s, \tilde{s}, \mathbf{p}) & \text{otherwise} \end{cases} = \begin{cases} \mathbf{C}(s, \mathbf{p}) & if \ |s| \leq \tilde{s} \\ \tilde{\mathbf{C}}(s, \tilde{s}, \mathbf{p}) & \text{otherwise} \end{cases} = \mathbf{E}(s, \tilde{s}, \mathbf{p}). \tag{15}$$

Now, recalling the scalability property of a Cb3D curve in [24], a Cb3D curve is scalable as follows $\lambda \mathbf{C}(s, \mathbf{p}) = \mathbf{C}(\lambda s, \lambda^{-2} \mathbf{p})$. Thus,

$$\lambda \mathbf{E}(s, \tilde{s}, \mathbf{p}) = \begin{cases} \lambda \mathbf{C}(s, \mathbf{p}) & if \ |s| \leq \lambda \tilde{s} \\ \lambda \tilde{\mathbf{C}}(s, \lambda \tilde{s}, \mathbf{p}) & \text{otherwise} \end{cases} = \begin{cases} \mathbf{C}(\lambda s, \lambda^{-2} \mathbf{p}) & if \ |s| \leq \lambda \tilde{s} \\ \tilde{\mathbf{C}}(\lambda s, \lambda \tilde{s}, \lambda^{-2} \mathbf{p}) & \text{otherwise} \end{cases} = \mathbf{E}(\lambda s, \lambda \tilde{s}, \lambda^{-2} \mathbf{p}). \tag{16}$$

6

■

The scalability property of Lemma III.2 allows us to design a curve for the unitary case $\tilde{s} = 1$ and then scale it, if necessary, by multiplying with the factor λ (to extend its length, which implies that curve parameters are indeed multiplied with a factor $\mu \leftarrow \lambda^{-2}\mu$ and $\rho \leftarrow \lambda^{-2}\rho$). As a consequence, the unitary curve can be approximated with a look-up table (LUT) up to a desired accuracy and evaluated in a *zero-cost* time. On the other hand, the symmetry property of Lemma III.2 allows us to implement only the half of the LUT, to save some memory resources.

Lemma III.3 (Tangent vector) *Tangent vector* $\mathbf{T}_E(s, \tilde{s}, \mathbf{p})$ *can be computed as follows:*

$$
\mathbf{T}_E(s, \tilde{s}, \mathbf{p}) := \begin{cases} \mathbf{T}(s, \mathbf{p}) & if \ |s| \leq \tilde{s} \\[2mm] \underbrace{\mathbf{R}_{\mathbf{T}(\tilde{s}, \mathbf{p})}(\pi)\mathbf{T}(s - 2\tilde{s}, \mathbf{p})}_{\tilde{\mathbf{T}}(s, \tilde{s}, \mathbf{p})} & otherwise \end{cases} \tag{17}
$$

In particular, the tangent vector evaluated at the end of the curve, that is $\mathbf{T}_E(\pm S, \rho, \mu)$ *with* $S = 2\tilde{s}$*, can be computed as:*

$$
\mathbf{T}_E(\pm S, \rho, \mu) = \begin{bmatrix} 2\cos^2(\theta(\tilde{s}, \rho))\cos^2(\Psi(\tilde{s}, \rho, \mu)) - 1 \\[2mm] \cos^2(\theta(\tilde{s}, \rho))\sin(2\Psi(\tilde{s}, \rho, \mu)) \\[2mm] -\sin(2\theta(\tilde{s}, \rho))\cos(\Psi(\tilde{s}, \rho, \mu)) \end{bmatrix} = \begin{bmatrix} 2\cos^2(\frac{\rho\tilde{s}^2}{2})\cos^2(\frac{\mu}{2}C^2(\tilde{s}, \rho)) - 1 \\[2mm] \cos^2(\frac{\rho\tilde{s}^2}{2})\sin(\mu C^2(\tilde{s}, \rho)) \\[2mm] -\sin(\rho\tilde{s}^2)\cos(\frac{\mu}{2}C^2(\tilde{s}, \rho)) \end{bmatrix}. \tag{18}
$$

Proof Tangent vector can be obtained from the vector corresponding to the first derivative of Eq. (9). It's unitary expression is simply computed as $\mathbf{T}(s, \mathbf{p}) = \frac{\mathbf{C}'(s, \mathbf{p})}{\|\mathbf{C}'(s, \mathbf{p})\|}$ for $|s| \leq \tilde{s}$ and for $|s| > \tilde{s}$ the tangent vector is computed as $\tilde{\mathbf{T}}(s, \tilde{s}, \mathbf{p}) := \frac{\tilde{\mathbf{C}}'(s, \tilde{s}, \mathbf{p})}{\|\tilde{\mathbf{C}}'(s, \tilde{s}, \mathbf{p})\|} = \frac{\mathbf{R}_{\mathbf{T}(\tilde{s}, \mathbf{p})}(\pi)\mathbf{C}'(s - 2\tilde{s}, \mathbf{p})}{\|\mathbf{R}_{\mathbf{T}(\tilde{s}, \mathbf{p})}(\pi)\mathbf{C}'(s - 2\tilde{s}, \mathbf{p})\|} = \mathbf{R}_{\mathbf{T}(\tilde{s}, \mathbf{p})}(\pi)\frac{\mathbf{C}'(s - 2\tilde{s}, \mathbf{p})}{\|\mathbf{C}'(s - 2\tilde{s}, \mathbf{p})\|} = \mathbf{R}_{\mathbf{T}(\tilde{s}, \mathbf{p})}(\pi)\mathbf{T}(s - 2\tilde{s}, \mathbf{p})$.

On the other hand, Eq. (7) is indeed a transformed Cb3D curve, where the term $\mathbf{C}(s - \text{sign}(s)2\tilde{s}, \mathbf{p})$ is the piece of the *original* curve. It can clearly be seen that for $s = \pm 2\tilde{s}$ the tangent vector is indeed coincident with X-axis $\mathbf{T}(0) = \mathbf{X} = [1\ 0\ 0]^T$. Thus, the rotation of $\mathbf{X}$ around $\mathbf{T}(\tilde{s}) = [T_x(\tilde{s})\ T_y(\tilde{s})\ T_z(\tilde{s})]^T$ is the vector:

$$
\mathbf{T}_E(\pm 2\tilde{s}) = \mathbf{R}_{\mathbf{T}(\tilde{s})}(\pi)\mathbf{X} = \begin{bmatrix} 2T_x^2(\tilde{s}) - 1 & 2T_x(\tilde{s})T_y(\tilde{s}) & 2T_x(\tilde{s})T_z(\tilde{s}) \end{bmatrix}^T. \tag{19}
$$

Therefore, replacing the elements of the tangent vector in Eq. (3) gives:

$$
\mathbf{T}_E(\pm S, \rho, \mu) = \begin{bmatrix} 2\cos^2(\theta(\tilde{s}))\cos^2(\Psi(\tilde{s})) - 1 & \cos^2(\theta(\tilde{s}))\sin(2\Psi(\tilde{s})) & -\sin(2\theta(\tilde{s}))\cos(\Psi(\tilde{s})) \end{bmatrix}^T. \tag{20}
$$

After some trivial trigonometric manipulations and substituting pitch $\theta(\tilde{s})$ and yaw $\Psi(\tilde{s})$ angles at the intermediate

7

point, given by Eq. (2), we get to Eq. (18). ■

Lemma III.3 allows to compute the pointing direction of the curve. Particularly, Eq. (18) provides the direction that an UAV following that curve will point given a set of parameters $\tilde{s}$, ρ and μ. Indeed, this is a supporting lemma for the next two lemmas, as well as for the design of the curve parameters.

Lemma III.4 (Pitch and yaw angles) *Pitch $\Psi_E(s, \tilde{s}, \mathbf{p})$ and yaw $\theta_E(s, \tilde{s}, \mathbf{p})$ can be computed as follows:*

$$
\theta_E(s, \tilde{s}, \mathbf{p}) := \begin{cases} \theta(s, \mathbf{p}) & if\ |s| \le \tilde{s} \\ -\arcsin \tilde{T}_z & otherwise \end{cases}, \quad \Psi_E(s, \tilde{s}, \mathbf{p}) := \begin{cases} \Psi(s, \mathbf{p}) & if\ |s| \le \tilde{s} \\ \arctan \frac{\tilde{T}_y}{\tilde{T}_x} & otherwise \end{cases}, \tag{21}
$$

where $\tilde{T}_x$, $\tilde{T}_y$ and $\tilde{T}_z$ are the elements of the tangent vector $\tilde{\mathbf{T}}(s, \tilde{\mathbf{p}})$ in Lemma III.3.

In particular, for intermediate angles $\theta(\tilde{s}) \in [-\frac{\pi}{4}, 0]$ and $\Psi(\tilde{s}) \in [0, \frac{\pi}{4}]$, yaw and pitch angles at the end of an ECb3D are:

$$
\theta(\tilde{s}) \ge \theta_E(2\tilde{s}) := \arcsin\left(\cos\Psi(\tilde{s})\sin(2\theta(\tilde{s}))\right) \in [-\frac{\pi}{2}, 0] \tag{22}
$$

$$
\Psi(\tilde{s}) \le \Psi_E(2\tilde{s}) := \arctan\left(\frac{\cos^2(\theta(\tilde{s}))\sin(2\Psi(\tilde{s}))}{2\cos^2(\theta(\tilde{s}))\cos^2(\Psi(\tilde{s})) - 1}\right) \in [0, \frac{3\pi}{4}]. \tag{23}
$$

Also, the inverse relation can be obtained. Given pitch $\theta_E(2\tilde{s}) \in [-\frac{\pi}{2}, 0]$ and yaw $\Psi_E(2\tilde{s}) \in [0, \frac{\pi}{2}]$ angles of an Elementary Clothoid-based 3D curve, the angles, that is $\theta(\tilde{s})$ and $\Psi(\tilde{s})$, of the primary Cb3D curve are:

$$
\theta_E(2\tilde{s}) \le \theta(\tilde{s}) := \arctan\left(\frac{\sin(\theta_E(2\tilde{s}))}{\sqrt{\cos^2(\theta_E(2\tilde{s})) + 2\cos(\theta_E(2\tilde{s}))\cos(\Psi_E(2\tilde{s})) + 1}}\right) \in [-\frac{\pi}{4}, 0] \tag{24}
$$

$$
\Psi_E(2\tilde{s}) \ge \Psi(\tilde{s}) := \arctan\left(\frac{\cos(\theta_E(2\tilde{s}))\sin(\Psi_E(2\tilde{s}))}{\cos(\Psi_E(2\tilde{s}))\cos(\theta_E(2\tilde{s})) + 1}\right) \in [0, \frac{\pi}{4}] \tag{25}
$$

Proof The orientation in $\mathcal{S}^3$ defined by the **TNB** basis of any space curve in $\mathbb{R}^3$ can be defined by Euler angles roll $\phi_E(s, \tilde{s})$, pitch $\theta_E(s, \tilde{s})$, yaw $\Psi_E(s, \tilde{s})$, expressed as $\mathbf{R}_E(s, \tilde{s}) = \mathbf{R}_z(\Psi_E(s, \tilde{s}))\mathbf{R}_y(\theta_E(s, \tilde{s}))\mathbf{R}_x(\phi_E(s, \tilde{s}))$. The corresponding X-axis of the local frame (first column of $\mathbf{R}_E(s, \tilde{s})$) is indeed the tangent vector, which depends on $\theta_E(s, \tilde{s})$ and $\Psi_E(s, \tilde{s})$ (similar to Eq. (3)):

$$
\mathbf{T}_E(\theta_E(s, \tilde{s}), \Psi_E(s, \tilde{s})) := \left[\cos(\Psi_E(s, \tilde{s}))\cos(\theta_E(s, \tilde{s})) \quad \sin(\Psi_E(s, \tilde{s}))\cos(\theta_E(s, \tilde{s})) \quad -\sin(\theta_E(s, \tilde{s}))\right]^T. \tag{26}
$$

Thus, combining Eqs. (17) and (26), we get to Eq. (21).

Now, from Eq. (18) we can get the angles for $s = 2\tilde{s}$, so comparing Eqs. (18) and (26), and after some trivial manipulations, we get Eqs. (22) and (23). It is worth noting that, for $\theta(\tilde{s}) \in [-\frac{\pi}{4}, 0]$ and $\Psi(\tilde{s}) \in [0, \frac{\pi}{4}]$, Eqs. (22) and
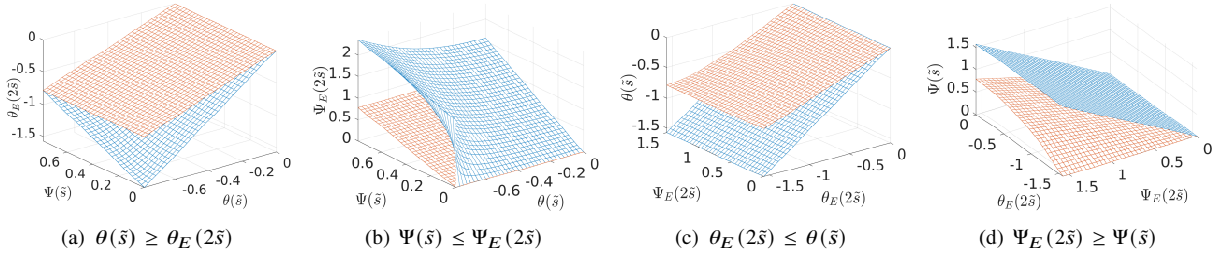
Fig. 2 (a)-(b) Pitch and yaw angles of an ECb3D curve (in blue) and (c)-(d) its inverse relations for a Cb3D curve (in red).

(23) provide values within ranges $\theta_E(2\tilde{s}) \in [-\frac{\pi}{2}, 0]$ and $\Psi_E(2\tilde{s}) \in [0, \frac{3\pi}{4}]$, because $\sin(\theta_E(2\tilde{s})) \in [-1, 0]$ (the minimum is given for $\theta(\tilde{s}) = -\frac{\pi}{4}$ and $\Psi(\tilde{s}) = 0$). On the other hand, the maximum for $\tan(\Psi_E(2\tilde{s}))$ is produced when $\theta(\tilde{s}) = -\frac{\pi}{4}$ and $\Psi(\tilde{s}) = \frac{\pi}{4}$, being $\Psi_E(2\tilde{s}) = \frac{3\pi}{4}$ for those values, see Fig. 2, in its (a) and (b) plots. Also note that $\theta(\tilde{s}) \geq \theta_E(2\tilde{s})$ and $\Psi(\tilde{s}) \leq \Psi_E(2\tilde{s})$. A similar prove could be done for $s = -2\tilde{s}$, since the curve is symmetric (Lemma III.2).

On the other hand, from Eq. (20) we can get primary Cb3D angles for a given target tangent vector $\mathbf{T}_E(2\tilde{s}) = [T_{E,x}\ T_{E,y}\ T_{E,z}]^T$ as follows:

$$\Psi(\tilde{s}) = \arctan\left(\frac{T_{E,y}}{T_{E,x} + 1}\right) \tag{27}$$

$$\theta(\tilde{s}) = \arctan\left(\frac{-T_{E,z}}{T_{E,y}}\sin\Psi(\tilde{s})\right) = \arctan\left(\frac{-T_{E,z}}{\sqrt{(T_{E,x})^2 + (T_{E,y})^2 + 2T_{E,x} + 1}}\right) \tag{28}$$

Now, using Eq. (26) and after some basic trigonometric manipulations, we can get to Eqs. (24) and (25). Figure 2, in its (c) and (d) plots, shows that pitch and yaw angles of the primary Cb3D are within the indicated ranges in Eqs. (24) and (25), and also that $\theta_E(2\tilde{s}) \leq \theta(\tilde{s})$ and $\Psi_E(2\tilde{s}) \geq \Psi(\tilde{s})$. ∎

Lemma III.4 states that for the given range of $\theta(\tilde{s}) \in [-\frac{\pi}{4}, 0]$ and $\Psi(\tilde{s}) \in [0, \frac{\pi}{4}]$ the value of final pitch angle of the Elementary curve is always smaller (also the opposite relation occurs, given $\theta_E(2\tilde{s}) \in [-\frac{\pi}{2}, 0]$ and $\Psi_E(2\tilde{s}) \in [0, \frac{3\pi}{4}]$ the intermediate pitch angle is always greater). A similar reasoning can be applied to the yaw angle.

IV. Analysis of ECb3D Monotony

The aim of this section is to analyse the regions of space where an ECb3D curve is monotonic in position and/or orientation (pitch and yaw angles). First, we study the necessary conditions such that the curve is monotonic in position.Afterwards, we focus on the orientation problem, which is more difficult to prove. Without loss of generality the study is made for the case where target angles $\theta_E^* \in [-\frac{\pi}{2}, 0]$ and $\Psi_E^* \in [0, \frac{\pi}{2}]$, that is the red curve in Fig. 1, but a similar proof can be made for the other cases.
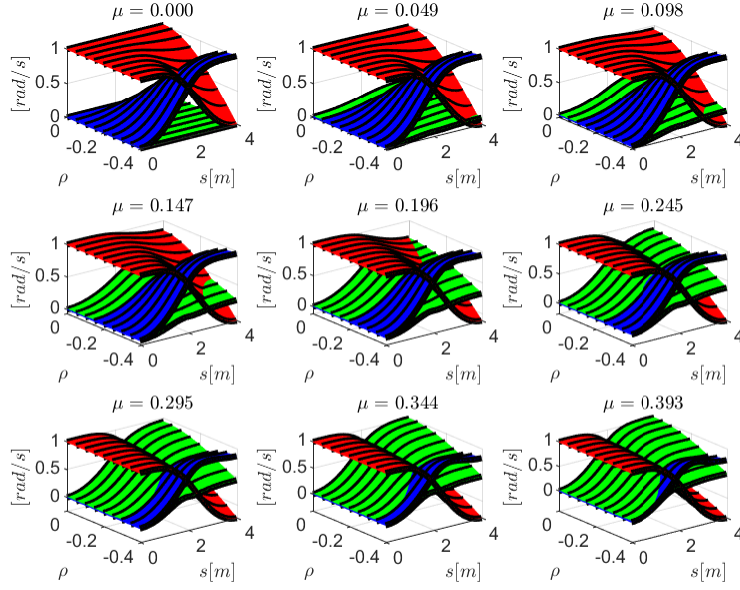
Fig. 3 **Elements of $\mathbf{T}_E(s, \tilde{s}, \mathbf{p})$ ($T_{x,E}(s)$ in red, $T_{y,E}(s)$ in green and $T_{z,E}(s)$ in blue) over a parametric sweep of $\rho \in [-\frac{\pi}{2}, 0]$ and $\mu \in [0, \frac{\pi}{2}]$ with $\tilde{s} = 1$.**

Lemma IV.1 (Monotonically increasing in position) *An Elementary Clothoid-based 3D curve monotonically increases its position over s if $\theta_E(s, \tilde{s}, \mathbf{p}) \in [-\frac{\pi}{2}, 0]$ and $\Psi_E(s, \tilde{s}, \mathbf{p}) \in [0, \frac{\pi}{2}]$.*

Proof The position vector of $\mathbf{E}(s, \tilde{s}, \mathbf{p})$ is monotonically increasing iff the elements of the tangent vector, as stated in Eq. (26) of Lemma III.3, are positive:

$$\mathbf{T}_E(s, \tilde{s}, \mathbf{p}) = \begin{cases} \cos(\Psi_E(s, \tilde{s}, \mathbf{p})) \cos(\theta_E(s, \tilde{s}, \mathbf{p})) \geq 0 \\ \sin(\Psi_E(s, \tilde{s}, \mathbf{p})) \cos(\theta_E(s, \tilde{s}, \mathbf{p})) \geq 0 \\ -\sin(\theta_E(s, \tilde{s}, \mathbf{p})) \geq 0 \end{cases} \quad (29)$$

We can clearly see that all elements of the tangent vector are always zero or greater than 0 for the given ranges $\theta_E(s, \tilde{s}, \mathbf{p}) \in [-\frac{\pi}{2}, 0]$ and $\Psi_E(s, \tilde{s}, \mathbf{p}) \in [0, \frac{\pi}{2}]$. ∎

Lemma IV.1 provides necessary conditions to ensure that the position increases monotonically. However, given arbitrary clothoid parameters ρ and μ, angles in Eq. (21) might outside the bounds indicated in Lemma III.4 for some s. This is shown in Fig. 3, where the elements of Eq. (17) have been obtained over s and a parametric sweep of $\rho \in [-\frac{\pi}{2}, 0]$ and $\mu \in [0, \frac{\pi}{2}]$ with $\tilde{s} = 1$. It can be seen that the X coordinate of the tangent vector can take negative values for some combinations of s, ρ and μ, while Y and Z coordinates are always positive. This implies that Ψ_E in Eq. (21) can take values greater than $\frac{\pi}{2}$ and thus the curve is not monotonic in X for those cases.

(a) Minimum of the X coordinate of the tangent vector.

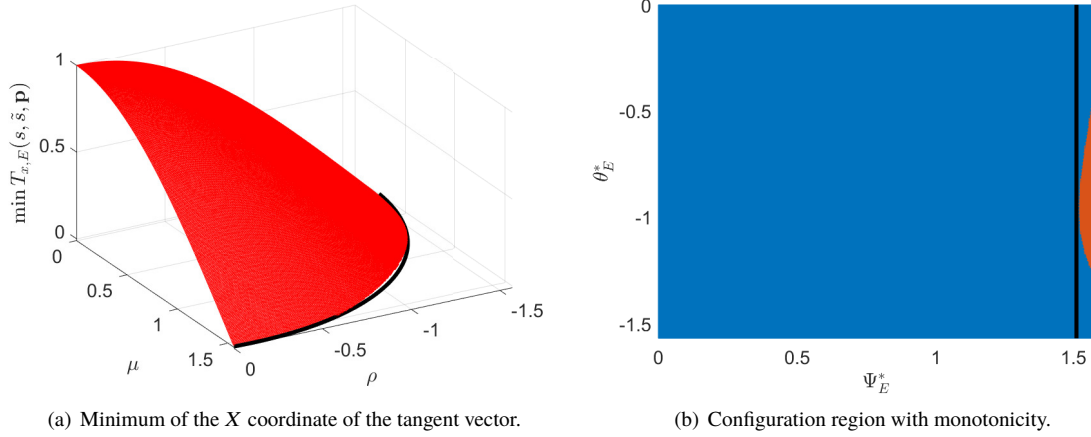(b) Configuration region with monotonicity.

Fig. 4   Analysis of the monotonicity of X.

Indeed, if we plot the minimum of the X element of the tangent vector (as shown in Fig. 4(a)), we can see that the following constraint (depicted in black in the figure) includes all the cases where the curve is monotonic in X:

$$\sqrt{\left(\frac{\rho^* \tilde{s}^2}{\pi/2}\right)^2 + \left(\frac{\mu^* \tilde{s}^2}{\pi/2}\right)^2 - \phi \left|\frac{\rho^* \tilde{s}^2}{\pi/2}\right| \left|\frac{\mu^* \tilde{s}^2}{\pi/2}\right|} < 1, \tag{30}$$

being $\phi = 0.15$ a parameter that has been experimentally adjusted by trial and error until all represented cases provide positive values for all elements of the tangent vector. Constraint in Eq. (30) can be expressed in terms of intermediate angles using Eqs. (4) and (5) independently of the value of $\tilde{s}$:

$$\sqrt{\left(\frac{2\theta^*}{\pi/2}\right)^2 + \left(\frac{2\Psi^*}{C^2(1, 2\theta^*)\pi/2}\right)^2 - \phi \left|\frac{2\theta^*}{\pi/2}\right| \left|\frac{2\Psi^*}{C^2(1, 2\theta^*)\pi/2}\right|} < 1. \tag{31}$$

Figure 4(b) represents the region of the target configuration space where the solution obtained increases monotonically in position (blue region), which basically covers the whole configuration space. This region has been obtained by replacing Eqs. (24) and (25) in Eq. (31). Based on this result, in a conservative option, we could bound Eq. (31) with $\Psi_E^* < 1.51$ rad (depicted as a black line in the figure) to ensure monotonicity.

11

Lemma IV.2 (Monotonically increasing in yaw) *An Elementary clothoid-based 3D curve monotonically increases its yaw angle over s if the final pitch and yaw angles are within the ranges $\theta_E(2\tilde{s}) \in [-\frac{\pi}{2}, 0]$ and $\Psi_E(2\tilde{s}) \in [0, \frac{\pi}{2}]$.*

Proof Yaw angle monotonically increases iff its derivative is positive, thus, recalling that $\Psi'(s) \geq 0$ for $|s| \leq \tilde{s}$ as demonstrated in [24], we need to check that the secondary Cb3D yaw angle also increases monotonically (Eq. (21) from Lemma III.4). Its derivative, for $|s| > \tilde{s}$, is computed as:

$$\tilde{\Psi}'_E(s, \tilde{s}) = \frac{\tilde{T}'_y(s, \tilde{s})\tilde{T}_x(s, \tilde{s}) - \tilde{T}'_x(s, \tilde{s})\tilde{T}_y(s, \tilde{s})}{\tilde{T}_x^2(s, \tilde{s}) + \tilde{T}_y^2(s, \tilde{s})}, \tag{32}$$

So if $\chi(s, \tilde{s}) := \tilde{T}'_y(s, \tilde{s})\tilde{T}_x(s, \tilde{s}) - \tilde{T}'_x(s, \tilde{s})\tilde{T}_y(s, \tilde{s}) \geq 0$, implies that $\tilde{\Psi}'_E(s, \tilde{s}) \geq 0$, which is true for the given ranges:

$$\chi(s, \tilde{s}) = \Big(\sin(2\theta(\tilde{s}))\sin(\Psi(s - 2\tilde{s}') - \Psi(\tilde{s}))\theta'(s - 2\tilde{s}) - \cos(2\theta(\tilde{s}))\cos^2(\theta(s - 2\tilde{s}))\Psi'(s - 2\tilde{s}) -$$
$$-\frac{1}{2}\sin(2\theta(\tilde{s}))\sin(2\theta(s - 2\tilde{s}))\cos(\Psi(s - 2\tilde{s}') - \Psi(\tilde{s}))\Psi'(s - 2\tilde{s})\Big) \geq 0, \tag{33}$$

since $\theta(\tilde{s}) \geq \theta_E(2\tilde{s})$, $\Psi(\tilde{s}) \leq \Psi(2\tilde{s})$ and the fact that $\sin(2\theta(\tilde{s})) \leq 0$, $\cos(2\theta(\tilde{s})) \geq 0$, $\sin(\Psi(s - 2\tilde{s}) - \Psi(\tilde{s})) \leq 0$, $\theta'(s - 2\tilde{s}) \geq 0$, $\Psi'(s - 2\tilde{s}) \leq 0$, $\sin(2\theta(s - 2\tilde{s})) \leq 0$, $\cos(\Psi(s - 2\tilde{s}) - \Psi(\tilde{s})) \geq 0$. ∎

Lemma IV.2 provides necessary conditions to obtain solutions where the rotation given by the yaw angles increases monotonically. However, we cannot guarantee that pitch angle decreases monotonically for the specified ranges. Indeed, there are cases, depending on ρ and μ, where the derivative of the angle for the secondary Cb3D takes positive values. This can be seen from the derivative of Eq. (22):

$$\tilde{\theta}'_E(s, \tilde{s}) = -\frac{\tilde{T}'_z(s, \tilde{s})}{\sqrt{1 - \tilde{T}_z^2}}, \quad \tilde{T}'_z(s, \tilde{s}) = \left(\begin{pmatrix} \sin(\theta(s - 2\tilde{s}))\sin(2\theta(\tilde{s}))\cos(\Psi(s - 2\tilde{s}) - \Psi(\tilde{s})) - \\ -\cos(\theta(s - 2\tilde{s}))(2\sin^2(\theta(\tilde{s})) - 1) \end{pmatrix}\theta'(s - 2\tilde{s}) + \\ + \big(\sin(\Psi(s - 2\tilde{s}) - \Psi(\tilde{s}))\sin(2\theta(\tilde{s}))\cos(\theta(s - 2\tilde{s}))\big)\Psi'(s - 2\tilde{s})\right) \geq 0, \tag{34}$$

where the terms multiplying $\theta'(s - 2\tilde{s})$ and $\Psi'(s - 2\tilde{s})$ are both positive, however $\theta'(s - 2\tilde{s}) \geq 0$ and $\Psi'(s - 2\tilde{s}) \leq 0$. As a consequence, there is no guarantee that $\tilde{T}'_z(s, \tilde{s})$ is positive for all s. Indeed, by definition, $\tilde{T}'_z(\tilde{s}, \tilde{s}) \geq 0$ because the primary Cb3D increases monotonically for those ranges, and $\tilde{T}'_z(2\tilde{s}, \tilde{s}) = 0$ since the ECb3D path's curvature and torsion are both zero when $s = 2\tilde{s}$. Therefore, depending on ρ and μ the derivative could take positive values.

This aspect is shown in Fig. 5, where a study has been conducted to represent the derivatives over s of yaw and pitch angles, $\tilde{\Psi}'_E(s, \tilde{s})$ and $\tilde{\theta}'_E(s, \tilde{s})$ respectively, and a parametric sweep of $\rho \in [-\frac{\pi}{2}, 0]$ and $\mu \in [0, \frac{\pi}{2}]$ with $\tilde{s} = 1$. It can be seen that there are combinations, particularly with large $|\rho|$ and $|\mu|$, that generate a slight increase of $\tilde{\theta}_E(s, \tilde{s})$ (positive values of its derivative depicted in blue in Fig. 5), while the derivative of $\Psi_E(s, \tilde{s})$ is always positive (as already proved
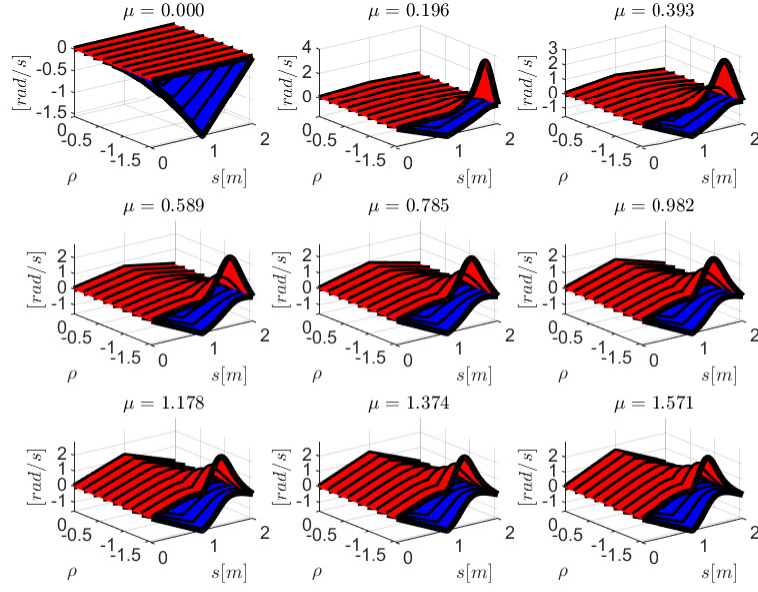
Fig. 5 Derivatives $\tilde{\Psi}'_E(s, \tilde{s})$ **(in red) and** $\tilde{\theta}'_E(s, \tilde{s})$ **(in blue) over a parametric sweep of** $\rho \in [-\frac{\pi}{2}, 0]$ **and** $\mu \in [0, \frac{\pi}{2}]$ **with** $\tilde{s} = 1$.

in Lemma IV.2). Varying the clothoid length would provide similar results. Indeed, if we use the scaling property of Lemma III.2, clothoid's parameter ranges need to be reduced by a factor of λ^{-2}, being λ the scaling factor, which produces a derivative scaled with λ^{-1} factor.

Inspired by this result, we seek now a region where pitch angle decreases monotonically. Figure 6(a) shows the maximum of $\tilde{\theta}'_E(s, \tilde{s})$ over a parametric sweep of $\rho \in [-\frac{\pi}{2\tilde{s}^2}, 0]$ and $\mu \in [0, \frac{\pi}{2\tilde{s}^2}]$ with $\tilde{s} = 1$. It can be seen that there is a wide region where the maximum is zero (which implies that pitch angle decreases monotonically). Due to the shape of this region, we have experimentally adjusted an ellipsoid that constrains solutions to ensure a monotonicity of pitch angle:

$$\sqrt{\left(\frac{\rho^*}{r_\rho}\right)^2 + \left(\frac{\mu^*}{r_\mu}\right)^2} < 1. \tag{35}$$

with $r_\rho = \frac{\pi}{2\tilde{s}^2}$ and $r_\mu = \frac{\varphi\pi}{2\tilde{s}^2}$, being $\varphi = 0.943277178$. The value for φ has been experimentally obtained by analysing all the cases depicted in Fig. 6(a) where the maximum derivative of the angle is zero. Replacing ρ^* and μ^* with Eqs. (4) and (5), respectively, then Eq. (35) can be equivalently expressed as:

$$\sqrt{\left(\frac{2\theta^*}{\pi/2}\right)^2 + \left(\frac{2\Psi^*}{\varphi\frac{\pi}{2}C^2(1, 2\theta^*)}\right)^2} < 1. \tag{36}$$

It is important to remark that Eq. (36) is independent of the clothoid arc length and sharpness parameters. The configuration region where this condition is satisfied is depicted in blue in Fig. 6(b). A conservative constraint would be
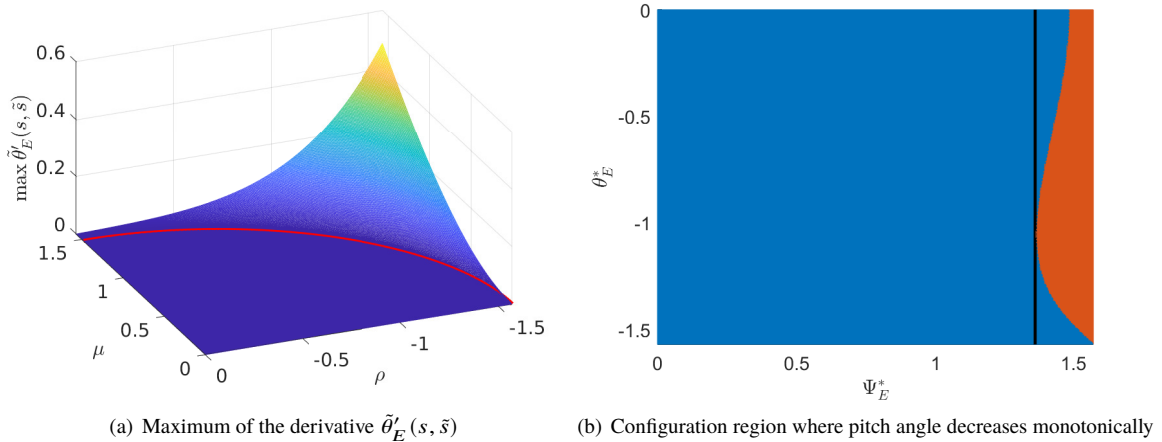
13

(a) Maximum of the derivative $\tilde{\theta}'_E(s, \tilde{s})$

(b) Configuration region where pitch angle decreases monotonically

Fig. 6   Analysis of the monotonicity of pitch angle.

to impose that $\Psi^*_E < 1.36$ rad (depicted as a black line in Fig. 6(b)).

V. Design Methodology Proposal

In this section we describe a design methodology to compute clothoid parameters ρ^* and μ^* based on target angles $\theta^*_E \in [-\frac{\pi}{2}, 0]$ rad and $\Psi^*_E \in [0, 1.36]$ rad, where admissible regions to ensure monotonicity have been taken into account as a result of the analysis performed in Section IV. An important aspect to consider is that we seek for solutions with the minimum possible curve length S, given admissible clothoid parameters $\rho^* \in [-\rho_{max}, \rho_{max}]$ and $\mu^* \in [-\mu_{max}, \mu_{max}]$. Thus, the length of the primary Cb3D, $\tilde{s}$, needs to be computed together with the clothoid parameters.

The methodology is based on the following steps:

1) Compute primary clothoid angles θ^* and Ψ^* from target angles θ^*_E and Ψ^*_E using Eqs. (24) and (25).

2) Then, assume that maximum torsion sharpness is applied, that is, $\rho^* = \text{sign}(\theta^*)\rho_{max}$. Thus, from Eq. (4), we compute the primary Cb3D length as:

$$\tilde{s}_{min} = \sqrt{\frac{2|\theta^*|}{\rho_{max}}}, \tag{37}$$

where $\tilde{s}_{min}$ is the shortest possible length (considering only the torsion sharpness constraint).

3) Compute μ^* using Eq. (5) assuming such length and previously computed yaw angle Ψ^*. If $|\mu^*| \leq \mu_{max}$, it means that the assumption about the maximum torsion solution was correct and then $\tilde{s}^* = \tilde{s}_{min}$. However, if $|\mu^*| > \mu_{max}$, it means that the primary Cb3D is too short, since it violates the admissible curvature sharpness, i.e.: torsion sharpness needs to be reduced. In that case, we now assume the maximum curvature sharpness is applied $\mu^* = \text{sign}(\Psi^*)\mu_{max}$. Using Eq. (5) we can compute the primary Cb3D length $\tilde{s}^*$, by replacing ρ^* of Eq. (4) into Eq. (5), that is $C(\tilde{s}, \rho^*) = C(\tilde{s}, \frac{2\theta^*}{\tilde{s}^2})$. Then, recalling the scalability property of Fresnel cosine, this term
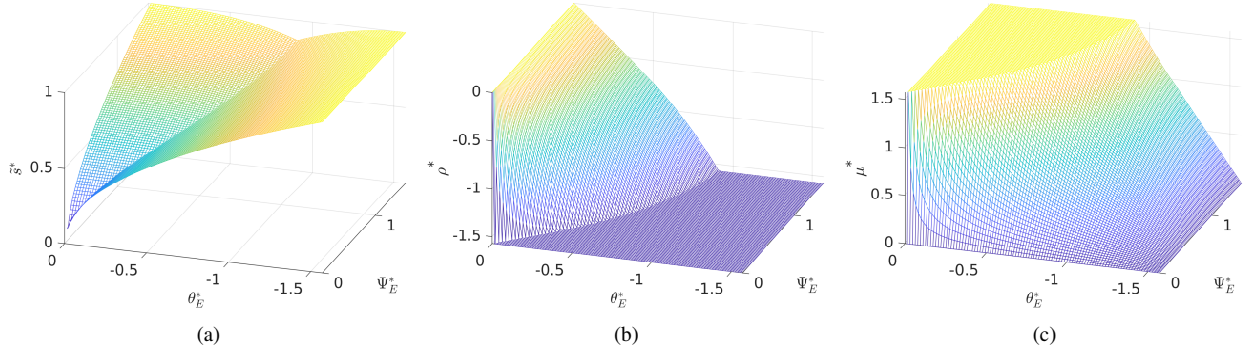
14

Fig. 7 Computed clothoid parameters using the proposed methodology.

can be computed as $C(\tilde{s}, \frac{2\theta^*}{\tilde{s}^2}) = C(1, 2\theta^*)\tilde{s}$. As a consequence, a proper clothoid length can be chosen to ensure that both sharpness constraints are satisfied:

$$\tilde{s}^* = \frac{\sqrt{\frac{2|\Psi^*|}{\mu_{max}}}}{C(1, 2\theta^*)}. \tag{38}$$

4) Compute torsion sharpness ρ^* using Eq. (4) and the previously computed length.

A. Case study

The proposed method finds clothoid parameters with the shortest possible length because it finds solutions trying to maximize clothoid sharpness (it selects the solution that first violates the maximum clothoid sharpness constraints). Figure 7 shows the computed values for $\tilde{s}^*$, ρ^* and μ^* using the proposed method, assuming that $\rho_{max} = \frac{\pi}{2}$ and $\mu_{max} = \frac{\pi}{2}$. These results were compared with a nonlinear optimization procedure (using `fmincon` function in Matlab®) where the curve with the shortest length, satisfying clothoid sharpness constraints, was found. As a result, the maximum error between both alternative procedures in the whole surface was 10^{-6}, but the optimization procedure takes about 100 times more to produce the same results.

Two particular cases of ECb3D curves are analyzed next. In the first one the solution obtained reaches the maximum torsion sharpness, whereas the second one provides the maximum curvature sharpness. In particular, if $\theta^* = -\frac{\pi}{4}$ and $\Psi^* = \frac{\pi}{4}$, we obtain $\rho^* = -\frac{\pi}{2}$, $\mu^* = 1.24511$ and $\tilde{s}^* = 0.731738$; while if $\theta^* = -\frac{\pi}{8}$ and $\Psi^* = 3\frac{\pi}{8}$, we obtain $\rho^* = -0.64818$, $\mu^* = \frac{\pi}{2}$ and $\tilde{s}^* = 0.85105$. Figure 8 represents these two curves, where it can clearly be seen that the parameters obtained for the curve depicted in solid blue imply a solution where torsion sharpness is maximum, while the curve depicted in dashed red provides a solution with maximum curvature sharpness. In both cases, the curves reach the specified angles.

It's worth mentioning that the average computational time to compute 200 points of the curve parameters is approximately 170μs (including clothoid parameters computation) based on our code implemented in Matlab® 2019b

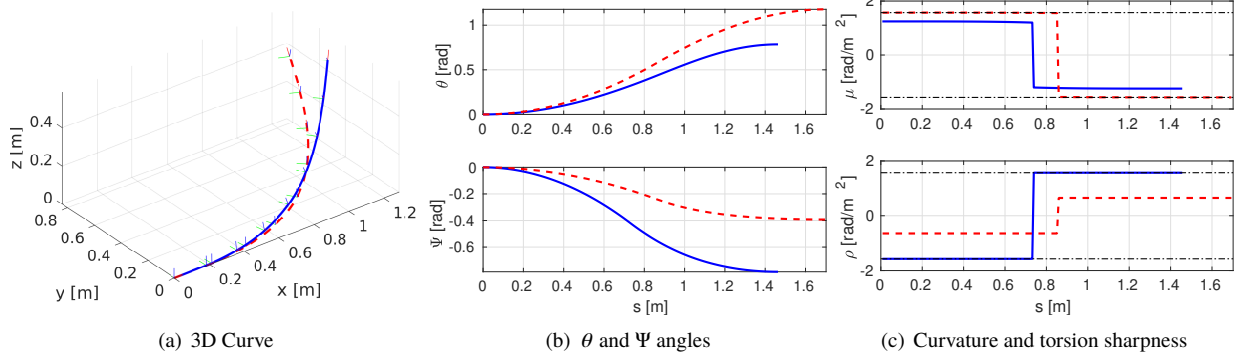(a) 3D Curve (b) θ and Ψ angles (c) Curvature and torsion sharpness

Fig. 8 Two representative Elementary Clothoid-based 3D curves, with final angles $\theta^* = -\frac{\pi}{4}$ and $\Psi^* = \frac{\pi}{4}$ (solid blue), and with final angles $\theta^* = -\frac{\pi}{8}$ and $\Psi^* = 3\frac{\pi}{8}$ (dashed red). Sharpness bounds appear in dash-dotted black.

running on computer with an Intel® Core i7-8750H processor and 16 GB of RAM memory and Windows 10.

B. Benchmarking

To complete the analysis of the proposed methodology, we have generated 10^4 random target orientations, Ψ^* and θ^*, comprised in the ranges $\Psi^* \in [0, \frac{\pi}{2}]$ rad and $\theta^* \in [0, \frac{\pi}{2}]$ rad, respectively. The aim is to compare some geometric properties, such as abruptness, maximum bending energy, as well as accuracy and computational time between our proposed curve (ECb3D) and an elementary curve consisting of two symmetric pure 3D clothoids (EC3D) [38]. EC3D are obtained after an optimization procedure where the curve sharpness parameters for curvature and torsion are adjusted so that the curve reaches the target orientations. In both cases, the length of the curves have been set to $S = 2$ m.

On the one hand, Fig. 9(a) depicts the histogram of the maximum bending energy of each curve $\max(\mathcal{B}(s))$, being $\mathcal{B}(s) := \kappa'^2(s) + \tau'^2(s)$ and $\kappa'(s)$ and $\tau'(s)$ the geometric derivatives of curve's curvature and torsion, respectively. In both cases, it can be seen that, in most cases, the proposed curve provides smaller bending energy (histogram cases are concentrated on the lower part of the chart). On the other hand, Fig. 9(b) shows the results obtained for the curve abruptness $\mathcal{A}(S) = \int_0^S \mathcal{B}(s)ds$, where it can be seen that ECb3D curve provides a solution with smaller abruptness.

The average computational time for computing curve parameters for a ECb3D is 28 μs, while computing an EC3D curve takes 121 ms in average. The superior performance is clearly influenced by the fact that the EC3D requires an optimization procedure in order to synthesize the curve. In addition to this, the proposed method is exact (errors are in the order of numerical accuracy), while the EC3D provides an approximated solution with an average error of 1 mrad, measured as $\epsilon := \sqrt{(\Psi^* - \Psi(S))^2 + (\theta^* - \theta(S))^2}$.

C. Fixed-wing UAV manoeuvres generation

The aim is to find a path for an UAV moving on a horizontal plane that manoeuvres to reach a target heading orientation $\Psi^* \in [-\pi, \pi]$ (relative to its current heading direction) on another horizontal plane ($\theta^* = 0$) at a different
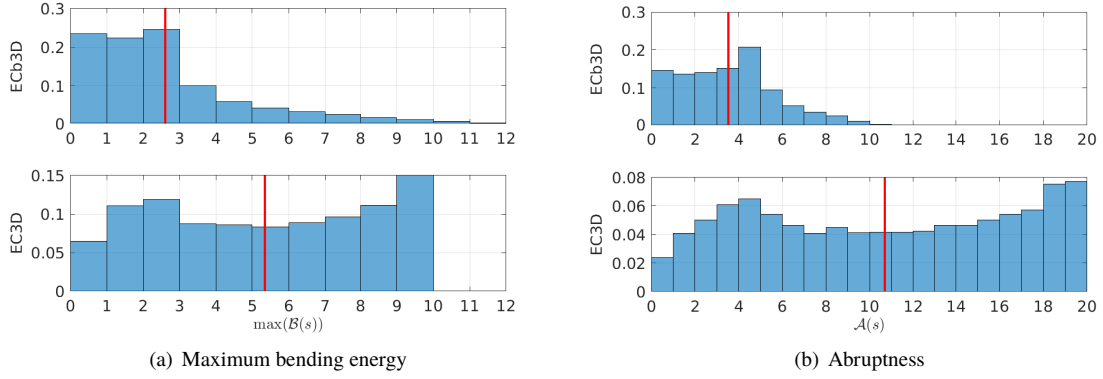
16

Fig. 9 Maximum bending energy and abruptness histograms to compare ECb3D and EC3D curves. Vertical axis represents parts per unit, where red lines show mean values for each metric.

altitude z^*, without exceeding the maximum allowed pitch angle $|\theta| < \theta_{max}$, and also considering maximum allowed sharpness in curvature and torsion, that is, $\rho \in [-\rho_{max}, \rho_{max}]$ and $\mu \in [-\mu_{max}, \mu_{max}]$. In order to solve this problem, we can use two concatenated ECb3D curves with intermediate heading orientation $\Psi_m^* = \frac{\Psi^*}{2}$ and $\theta_m^* = -\text{sign}(z^*)\theta_{max}$. These angles will be the actual target angles to reach with the first ECb3D curve (as explained at the beginning of this section). Then, we compute relative pitch and yaw angles required for the second ECb3D by computing the relative rotation matrix $\mathbf{R}_m^* = (\mathbf{R}_z(\Psi_m^*)\mathbf{R}_y(\theta_m^*))^{-1}(\mathbf{R}_z(\Psi^*)\mathbf{R}_y(\theta^*))$, details left to the reader.

Due to the assumption that the first ECb3D produces a curve with a maximum or minimum pitch angle, i.e.: $\theta_m^* = \theta_{max}$ or $\theta_m^* = -\theta_{max}$, this implies that the curve reaches a minimum altitude change z_{min}. Thus, if $|z^*| > z_{min}$, then the curve can be scaled by a factor $\lambda = (\frac{z_{min}}{z^*})^2$. On the contrary, if $|z^*| < z_{min}$, then we need to find the pitch angle that produces the required height (using any optimization method). The resulting solution produces a curve that reaches z^* with the maximum sharpness parameters.

Figure 10(a) shows three cases of two concatenated ECb3D curves generating manoeuvres with $\Psi^* = \frac{\pi}{2}$ heading at different altitudes with $\rho_{max} = \mu_{max} = 0.001$ rad/m^2 and $\theta_{max} = 0.6$ rad. In particular, we show in green the case where, due to the given constraints, the target altitude is equal to z_{min}. The curve plotted in red represents a case where $z^* < z_{min}$, while the curve plotted in blue represents a case where $z^* > z_{min}$. It can be seen that minimum pitch angle for green and blue curves is $min(\theta) = -0.6$ rad, expected by design (the blue one reaches a higher altitude by scaling the ECb3D parameters). The minimum pitch angle for the red curve is bigger than $-\theta_{max}$ as a consequence of an optimization procedure that makes the curve reach the target altitude.

VI. Discussion

Smooth spatial paths for autonomous aerial vehicles are usually generated using Bezier curves, splines or Pythagorean Hodographs, among other curves [20–22, 42]. However, they do not have a clear physical meaning or require to solve
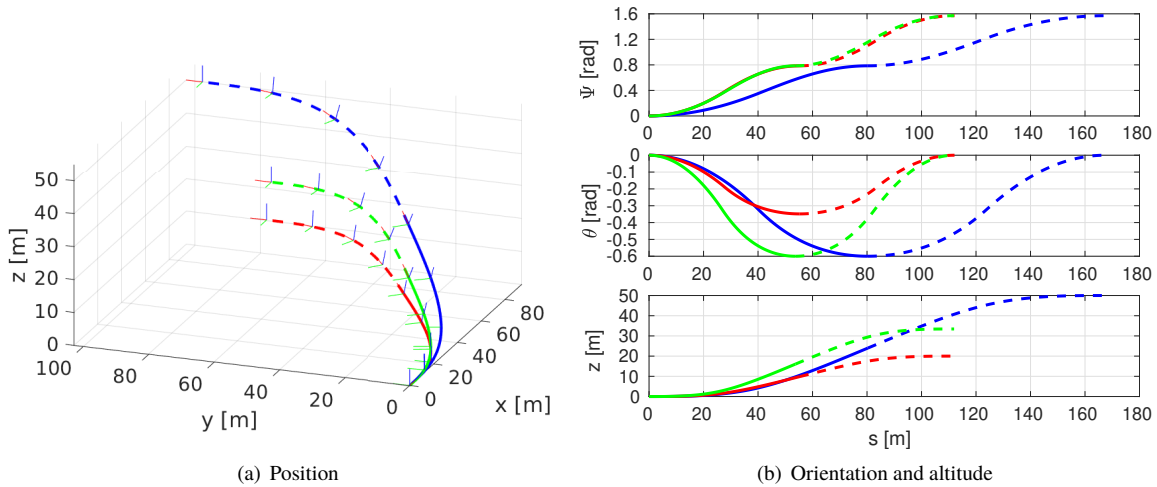
(a) Position   (b) Orientation and altitude

Fig. 10   **Three paths with two concatenated ECb3D curves each, with $\rho_{max} = \mu_{max} = 0.001$ rad/m^2 and $\theta_{max} = 0.6$, reaching final orientation $\Psi^* = \frac{\pi}{2}$ rad and different altitudes $z^* = 20$ m (red), $z^* = 33.44 = z_{min}$ m (green) and $z^* = 50$ m (blue).**

an optimization problem in order to take geometric, kinematic or dynamic constraints into account [21, 22]. The curve proposed in this Note inherits the properties from the Clothoid-based 3D curves introduced in [24] and, therefore, it has a physical meaning as its design parameters are related to curvature and torsion sharpness. ECb3D paths can be computed using optimization-free approximation methods [43–45] based on Bezier, splines or polynomial curves, among others. ECb3D paths are smooth and scalable, which make them suitable for many UAV navigation applications.

Some potential applications of the proposed Elementary Clothoid-based 3D curve are the following. Firstly, ECb3D curves can be used as transition curves in global path planning problems defining a poly-line in the workspace. Using ECb3D as a transition curve between segments will avoid the intrinsic C^1 discontinuity. Secondly, ECb3D curves can be integrated in local path planning methods to avoid obstacles by generating random motion primitives pointing to different directions. Collision tests could be performed and the collision-free ones would be selected as candidate solutions, where the final decision would depend on specific optimization criteria. Finally, ECb3D curves can also be used as a primitive in UAVs planning problems, combining straight segments, arcs and transition curves as part of their set of primitives. For instance, specific planning problems, such as changing the direction and altitude of a fixed-wing UAV, can benefit from the use of ECb3D curves by combining two of them as shown in section V.C.

VII. Conclusions

In this Note, we have proposed a new curve by concatenating two symmetric Clothoid-based 3D curves (Cb3D). We have proved that the new curve keeps the same properties regarding smoothness, scalability and symmetry as the original Cb3D curves. One of the main advantages of the new curve, compared to Cb3D, is that curvature and torsion

are zero, both at the beginning and at the end of the path, which makes it easier to combine with straight line segments and use them as transition curves to change the direction, while satisfying curvature and torsion sharpness constraints, i.e.: to ensure that transitions are smooth and compliant with some higher-level kinematic and dynamic constraints.

This Note also shows how to obtain curve parameters given the curve length, as well as how to compute pitch and yaw angles at the end of the curve and at the intermediate position. We also analyze the range of target pitch and yaw angles that ensures that the proposed curve increases monotonically in position and orientation, which is a desirable property for transition curves.

A method to obtain the shortest possible curve satisfying parameter constraints has also been proposed in section V. We also show a case study where fundamental variables of the curve are depicted and a comparison between the proposed curve and the curve in [38] has been conducted. The benchmarking concludes that the proposed curve generates smoother paths in the majority of the cases, with reduced bending energy and abruptness. The computational time and error are clearly smaller due to the closed-form solution presented.

At the end of the Note, we discuss why ECb3D paths are suitable for many UAV navigation applications. The main conclusions are that smoothness and scalability properties, as well as accuracy and reduced computation time, allow the use of ECb3D paths as primitive curves for higher level 3D path planners.

Further work will be oriented to generalize the problem statement to design curves that join two arbitrary positions and orientations in the configuration space, for instance, by combining ECb3D curves with line segments and helix curves extending the ideas of [46] to 3D.

Funding Sources

References

[1] Afman, J.-P., Ciarletta, L., Feron, E., Franklin, J., Gurriet, T., and Johnson, E. N., "Towards a new paradigm of UAV safety," *arXiv preprint arXiv:1803.09026*, 2018.

[2] Baek, H., and Lim, J., "Design of Future UAV-Relay Tactical Data Link for Reliable UAV Control and Situational Awareness," *IEEE Communications Magazine*, Vol. 56, No. 10, 2018, pp. 144–150. https://doi.org/10.1109/MCOM.2018.1700259.

[3] Varshosaz, M., Afary, A., Mojaradi, B., Saadatseresht, M., and Ghanbari Parmehr, E., "Spoofing Detection of Civilian UAVs Using Visual Odometry," *ISPRS International Journal of Geo-Information*, Vol. 9, No. 1, 2020. https://doi.org/10.3390/ijgi9010006.

[4] Hartmann, K., and Giles, K., "UAV exploitation: A new domain for cyber power," *2016 8th International Conference on Cyber Conflict (CyCon)*, 2016, pp. 205–221. https://doi.org/10.1109/CYCON.2016.7529436.

[5] Orfanus, D., de Freitas, E. P., and Eliassen, F., "Self-Organization as a Supporting Paradigm for Military UAV Relay Networks," *IEEE Communications Letters*, Vol. 20, No. 4, 2016, pp. 804–807. https://doi.org/10.1109/LCOMM.2016.2524405.

[6] Mualla, Y., Najjar, A., Daoud, A., Galland, S., Nicolle, C., Yasar, A.-U.-H., and Shakshuki, E., "Agent-based simulation of unmanned aerial vehicles in civilian applications: A systematic literature review and research directions," *Future Generation Computer Systems*, Vol. 100, 2019, pp. 344–364. https://doi.org/https://doi.org/10.1016/j.future.2019.04.051.

[7] Löbl, D., Holzapfel, F., Weiss, M., and Shima, T., "Cooperative Docking Guidance and Control with Application to Civil Autonomous Aerial Refueling," *Journal of Guidance, Control, and Dynamics*, 2021, pp. 1–11. https://doi.org/10.2514/1. G004425.

[8] Islam, M. S., Ahmed, M. M., and Islam, S., "A conceptual system architecture for countering the civilian unmanned aerial vehicles threat to nuclear facilities," *International Journal of Critical Infrastructure Protection*, Vol. 23, 2018, pp. 139–149. https://doi. org/https://doi.org/10.1016/j.ijcip.2018.10.003, URL https://www.sciencedirect.com/science/article/pii/S1874548217300124.

[9] Liu, C. H., Chen, Z., Tang, J., Xu, J., and Piao, C., "Energy-Efficient UAV Control for Effective and Fair Communication Coverage: A Deep Reinforcement Learning Approach," *IEEE Journal on Selected Areas in Communications*, Vol. 36, No. 9, 2018, pp. 2059–2070. https://doi.org/10.1109/JSAC.2018.2864373.

[10] Mo, H., and Farid, G., "Nonlinear and adaptive intelligent control techniques for quadrotor UAV–a survey," *Asian Journal of Control*, Vol. 21, No. 2, 2019, pp. 989–1008. https://doi.org/10.1002/asjc.1758.

[11] Nicotra, M. M., Naldi, R., and Garone, E., "Nonlinear control of a tethered UAV: The taut cable case," *Automatica*, Vol. 78, 2017, pp. 174–184. https://doi.org/https://doi.org/10.1016/j.automatica.2016.12.018, URL https://www.sciencedirect.com/ science/article/pii/S000510981630526X.

[12] Roberge, V., Tarbouchi, M., and Labonté, G., "Fast Genetic Algorithm Path Planner for Fixed-Wing Military UAV Using GPU," *IEEE Transactions on Aerospace and Electronic Systems*, Vol. 54, No. 5, 2018, pp. 2105–2117. https://doi.org/10.1109/TAES. 2018.2807558.

[13] Finger, D. F., Braun, C., and Bil, C., "A review of configuration design for distributed propulsion transitioning VTOL aircraft," *Asia-Pacific International Symposium on Aerospace Technology-APISAT*, 2017, pp. 3–5.

[14] Çakici, F., and Leblebicioğlu, M. K., "Control System Design of a Vertical Take-off and Landing Fixed-Wing UAV," *IFAC-PapersOnLine*, Vol. 49, No. 3, 2016, pp. 267–272. https://doi.org/10.1016/j.ifacol.2016.07.045, 14th IFAC Symposium on Control in Transportation Systems 2016.

[15] Liu, C., and Chen, W.-H., "Disturbance rejection flight control for small fixed-wing unmanned aerial vehicles," *Journal of Guidance, Control, and Dynamics*, Vol. 39, No. 12, 2016, pp. 2810–2819. https://doi.org/10.2514/1.G001958.

[16] Guclu, A., Kurtulus, D. F., and Arikan, K. B., "Attitude and altitude stabilization of fixed wing VTOL unmanned air vehicle," *AIAA Modeling and Simulation Technologies Conference*, 2016, p. 3378. https://doi.org/10.2514/6.2016-3378.

[17] Floreano, D., Zufferey, J.-C., Klaptocz, A., Germann, J., and Kovac, M., *Aerial Locomotion in Cluttered Environments*, Springer International Publishing, Cham, 2017, pp. 21–39. https://doi.org/10.1007/978-3-319-29363-9_2.

[18] Hong, H., Maity, A., Holzapfel, F., and Tang, S., "Model Predictive Convex Programming for Constrained Vehicle Guidance," *IEEE Transactions on Aerospace and Electronic Systems*, Vol. 55, No. 5, 2019, pp. 2487–2500. https://doi.org/10.1109/TAES.2018.2890375.

[19] Hong, H., Piprek, P., Gerdts, M., and Holzapfel, F., "Computationally Efficient Trajectory Generation for Smooth Aircraft Flight Level Changes," *Journal of Guidance, Control, and Dynamics*, Vol. 44, No. 8, 2021, pp. 1532–1540. https://doi.org/10.2514/1.G005529, URL https://doi.org/10.2514/1.G005529.

[20] Wang, X., Jiang, P., Li, D., and Sun, T., "Curvature Continuous and Bounded Path Planning for Fixed-Wing UAVs," *Sensors*, Vol. 17, No. 9, 2017. https://doi.org/10.3390/s17092155.

[21] Neto, A. A., Macharet, D. G., and Campos, M. F., "Feasible path planning for fixed-wing UAVs using seventh order Bézier curves," *Journal of the Brazilian Computer Society*, Vol. 19, No. 2, 2013, pp. 193–203. https://doi.org/10.1007/s13173-012-0093-3.

[22] Vinokursky, D. L., Mezentceva, O. S., and Samoylov, P. V., "Trajectory Planning of UAV Group: Pythagorean Hodograph and Bernstein-Bezier Composite Curves in the Plane," *2020 International Russian Automation Conference (RusAutoCon)*, 2020, pp. 704–707. https://doi.org/10.1109/RusAutoCon49822.2020.9208121.

[23] Çelik, S. S., Yayli, Y., and Güler, E., "ON GENERALIZED EULER SPIRALS IN E^3." *International Journal of Geometry*, Vol. 5, No. 1, 2016.

[24] Girbés, V., Vanegas, G., and Armesto, L., "Clothoid-Based Three-Dimensional Curve for Attitude Planning," *Journal of Guidance, Control, and Dynamics*, Vol. 42, No. 8, 2019, pp. 1886–1898. https://doi.org/10.2514/1.G003551.

[25] Fraichard, T., and Scheuer, A., "From Reeds and Shepp's to continuous-curvature paths," *Robotics and Automation, IEEE Transactions on*, Vol. 20, No. 6, 2004, pp. 1025–1035. https://doi.org/10.1109/TRO.2004.833789.

[26] Alia, C., Gilles, T., Reine, T., and Ali, C., "Local trajectory planning and tracking of autonomous vehicles, using clothoid tentacles method," *2015 IEEE Intelligent Vehicles Symposium (IV)*, 2015, pp. 674–679. https://doi.org/10.1109/IVS.2015.7225762.

[27] Girbés, V., Armesto, L., and Tornero, J., "Path following hybrid control for vehicle stability applied to industrial forklifts," *Robotics and Autonomous Systems*, Vol. 62, No. 6, 2014, pp. 910–922. https://doi.org/10.1016/j.robot.2014.01.004.

[28] Lima, P. F., Trincavelli, M., Mårtensson, J., and Wahlberg, B., "Clothoid-Based Speed Profiler and Control for Autonomous Driving," *2015 IEEE 18th International Conference on Intelligent Transportation Systems*, 2015, pp. 2194–2199. https://doi.org/10.1109/ITSC.2015.354.

[29] Arshad, S., Sualeh, M., Kim, D., Nam, D. V., and Kim, G.-W., "Clothoid: An Integrated Hierarchical Framework for Autonomous Driving in a Dynamic Urban Environment," *Sensors*, Vol. 20, No. 18, 2020. https://doi.org/10.3390/s20185053.

[30] Kim, Y., Park, J. B., Son, W., and Yoon, T., "Modified turn algorithm for motion planning based on clothoid curve," *Electronics Letters*, Vol. 53, No. 24, 2017, pp. 1574–1576.

[31] Sedighi, S., Nguyen, D.-V., and Kuhnert, K.-D., "A New Method of Clothoid-Based Path Planning Algorithm for Narrow Perpendicular Parking Spaces," *Proceedings of the 5th International Conference on Mechatronics and Robotics Engineering*, Association for Computing Machinery, New York, NY, USA, 2019, p. 50–55. https://doi.org/10.1145/3314493.3314512.

[32] Horváth, E., and Pozna, C. R., "Clothoid-based Trajectory Following Approach for Self-driving vehicles," *2021 IEEE 19th World Symposium on Applied Machine Intelligence and Informatics (SAMI)*, 2021, pp. 000251–000254. https://doi.org/10.1109/SAMI50585.2021.9378664.

[33] Wilde, D. K., "Computing clothoid segments for trajectory generation," *2009 IEEE/RSJ International Conference on Intelligent Robots and Systems*, 2009, pp. 2440–2445. https://doi.org/10.1109/IROS.2009.5354700.

[34] Gim, S., Adouane, L., Lee, S., and Derutin, J.-P., "Clothoids composition method for smooth path generation of car-like vehicle navigation," *Journal of Intelligent & Robotic Systems*, Vol. 88, No. 1, 2017, pp. 129–146. https://doi.org/10.1007/s10846-017-0531-8.

[35] McCrae, J., and Singh, K., "Sketching piecewise clothoid curves," *Computers & Graphics*, Vol. 33, No. 4, 2009, pp. 452–461. https://doi.org/10.1016/j.cag.2009.05.006.

[36] Xiao, Q.-B., Wan, M., Liu, Y., Qin, X.-B., and Zhang, W.-H., "Space corner smoothing of CNC machine tools through developing 3D general clothoid," *Robotics and Computer-Integrated Manufacturing*, Vol. 64, 2020, p. 101949. https://doi.org/10.1016/j.rcim.2020.101949.

[37] Wan, T. R., Tang, W., and Chen, H., "A real-time 3D motion planning and simulation scheme for nonholonomic systems," *Simulation Modelling Practice and Theory*, Vol. 19, No. 1, 2011, pp. 423–439. https://doi.org/10.1016/j.simpat.2010.08.002, modeling and Performance Analysis of Networking and Collaborative Systems.

[38] Harary, G., and Tal, A., "3D Euler spirals for 3D curve completion," *Computational Geometry*, Vol. 45, No. 3, 2012, pp. 115–126. https://doi.org/10.1016/j.comgeo.2011.10.001.

[39] Fu, Z., Yu, J., Xie, G., Chen, Y., and Mao, Y., "A Heuristic Evolutionary Algorithm of UAV Path Planning," *Wireless Communications and Mobile Computing*, Vol. 2018, 2018, pp. 1–11. https://doi.org/10.1155/2018/2851964.

[40] Scheuer, A., and Fraichard, T., "Planning continuous-curvature paths for car-like robots," *Proceedings of IEEE/RSJ International Conference on Intelligent Robots and Systems. IROS '96*, Vol. 3, 1996, pp. 1304–1311 vol.3. https://doi.org/10.1109/IROS.1996.568985.

[41] Dai, J. S., "Euler–Rodrigues formula variations, quaternion conjugation and intrinsic connections," *Mechanism and Machine Theory*, Vol. 92, 2015, pp. 144–152. https://doi.org/10.1016/j.mechmachtheory.2015.03.004.

[42] Pfeifle, O., and Fichter, W., "Cascaded Incremental Nonlinear Dynamic Inversion for Three-Dimensional Spline-Tracking with Wind Compensation," *Journal of Guidance, Control, and Dynamics*, 2021, pp. 1–13. https://doi.org/10.2514/1.G005785.

[43] Sánchez-Reyes, J., and Chacón, J., "Polynomial approximation to clothoids via s-power series," *Computer-Aided Design*, Vol. 35, No. 14, 2003, pp. 1305–1313. https://doi.org/10.1016/S0010-4485(03)00045-9.

[44] Montes, N., Herraez, A., Armesto, L., and Tornero, J., "Real-time clothoid approximation by Rational Bezier curves," *2008 IEEE International Conference on Robotics and Automation*, 2008, pp. 2246–2251. https://doi.org/10.1109/ROBOT.2008.4543548.

[45] Meek, D., and Walton, D., "An arc spline approximation to a clothoid," *Journal of Computational and Applied Mathematics*, Vol. 170, No. 1, 2004, pp. 59–77. https://doi.org/10.1016/j.cam.2003.12.038.

[46] Scheuer, A., and Fraichard, T., "Collision-free and continuous-curvature path planning for car-like robots," *IEEE Int. Conf. on Robotics and Automation*, 1997, pp. 867–873 vol.1.